

Large-Scale, Uniform-Patterned CsCu₂I₃ Films for Flexible Solar-Blind Photodetectors Array with Ultraweak Light Sensing

Qiuchun Lu, Yufei Zhang, Guanlin Yang, Meiling Xiong, Wenqiang Wu, Zhangsheng Xu, Hui Lu, Yegang Liang, Zeping He, Yang Yu, Xiaoming Mo, Xun Han,* and Caofeng Pan*

Cesium copper halide perovskite is one of the promising materials for solar-blind light detection. However, most of the cesium copper halide perovskite-based photodetectors (PDs) are focused on ultraviolet A detection and realized on the rigid substrate in the single device configuration. Here, a flexible solar-blind PDs array (10 × 10 pixels) based on the CsCu₂I₃ film patterns for ultraweak light sensing and light distribution imaging is reported. Large-scale CsCu₂I₃ film arrays are synthesized with various shapes and uniform dimensions through a simple vacuum-heating-assisted solution method. Benefiting from excellent air stability and superior resistance to the photodegrading of the CsCu₂I₃ film, the array device exhibits long-term stable photoswitching behavior for 8 h and ultralow light detection capability to resolve the light intensity of 6.1 nW cm⁻² with a high responsivity of 62 A W⁻¹, and the array device can acquire clear images of “G”, “X”, and “U” showing the input light distribution. Moreover, the flame detection and warning system based on a curved solar-blind PDs array is demonstrated, which can be used for multi-flame monitoring and locating. These results can encourage potential applications of the CsCu₂I₃ film-based PDs array in the field of optical communication and environment monitoring.

passes through the atmosphere, the UVC light couldn't reach the earth's surface due to the strong absorption by the ozone sphere.^[2] Therefore, the UVC region, also known as the “solar-blind” waveband, which on earth is often generated from artificial light sources. Benefiting from ultra-low background interference, solar-blind PDs demonstrate excellent specificity in various applications, including space communication, flame detection, ozone hole monitoring, and missile warning.^[3,4] The ultrawide-bandgap semiconductors, such as AlGaN and ZnMgO, have been extensively investigated in the deep UV PDs owing to their high absorption coefficients,^[5,6] and high responsivity has been achieved in the corresponding phototransistors.^[7–9] However, the alloying synthetic process of these materials is complex and expensive. High Al and Mg composition ratios in these AlGaN and ZnMgO alloys can reduce the crystal quality and lead to phase separation.^[10,11]

Ga₂O₃ bulk and films have been demonstrated to be promising candidates for UVC sensing due to their direct wide band gap, excellent thermal and chemical stability.^[12–17] But their intrinsic persistent photoconductivity phenomenon

1. Introduction

Ultraviolet C (UVC) is a subregion of UV radiation with a wavelength ranging from 200 to 280 nm.^[1] As solar radiation

Q. Lu, M. Xiong, Y. Liang, Y. Yu, X. Mo, C. Pan
Center on Nanoenergy Research
School of Physical Science and Technology
Guangxi University
Nanning 530004, P. R. China
E-mail: cfpan@binn.cas.cn

Q. Lu, Y. Zhang, Z. Xu, H. Lu, Y. Liang, Z. He, Y. Yu, C. Pan
CAS Center for Excellence in Nanoscience
Beijing Key Laboratory of Micro-nano Energy and Sensor
Beijing Institute of Nanoenergy and Nanosystems
Chinese Academy of Sciences
Beijing 101400, P. R. China

Y. Zhang, Z. Xu, H. Lu, Z. He, C. Pan
School of Nanoscience and Technology
University of Chinese Academy of Sciences
Beijing 100049, P. R. China

G. Yang
College of Materials Science and Engineering
Hunan University
Changsha 410082, P. R. China

W. Wu, C. Pan
Institute of Microscale Optoelectronics
Shenzhen University
Shenzhen 518060, P. R. China

X. Han
ZJU-Hangzhou Global Scientific and Technological Innovation Center
School of Micro-Nano Electronics
Zhejiang University
Hangzhou 311200, P. R. China
E-mail: xunhan@zju.edu.cn

 The ORCID identification number(s) for the author(s) of this article can be found under <https://doi.org/10.1002/smll.202300364>.

DOI: 10.1002/smll.202300364

leads to a slow response speed and poor weak light detection capability. In addition, it requires high temperature and high vacuum growth conditions, which limits its applications in flexible integrated array devices. Considering the weak UVC light signals, the high performance solar-blind PDs with high responsivity and low power density detection limit are urgently expected.

Organic–inorganic hybrid lead halide perovskites have been emerging as a new generation of semiconducting materials,^[18–20] which exhibit superior optoelectronic properties, including high absorption coefficients and carrier mobility, long carrier diffusion length, and tunable optical bandgaps,^[21–25] making it possible to prepare the high-performance optoelectronic devices.^[26–28] To avoid the inherent toxicity of Pb-based perovskites, inorganic cesium copper halides are widely investigated as perovskite derivatives.^[29,30] The past five years have witnessed various applications of the Cs–Cu–I system in light-emitting diodes,^[31,32] artificial synapses,^[33] X-ray or γ -ray scintillator,^[34,35] and UV PDs.^[36] Furthermore, compared with Pb-based perovskite PDs being operated in the visible spectrum, the copper halide compound of CsCu₂X₃ or Cs₃Cu₂X₅ (X = I, Br, Cl) show the strong absorption of the solar-blind spectrum due to their inherent broadband gap.^[37] For example, CsCu₂I₃ and Cs₃Cu₂I₅ show the band edge in the absorption spectra ~285 and ~320 nm.^[29] Cs₃Cu₂I₅ film devices show obvious sensitivity to UV light from 265 to ~400 nm but are almost blind to visible light at 405 nm.^[38] And Cs₃Cu₂I₅/ β -Ga₂O₃ heterojunction PDs exhibit solar-blind UV response characteristics.^[39] These PDs reported salient performance in high-power density conditions with rigid substrates in the single device configuration. Endowing solar-blind PDs with high flexibility and array structure will certainly be important for the research and market of portable and wearable deep UV monitoring and imaging. And the wide UVC power density detection range promises the flexible solar-blind PDs' unique applications in flame alert and high signal-to-noise optical communications, etc.

Here, we demonstrate a flexible solar-blind PDs array (10 × 10 pixels) based on the high-quality lead-free CsCu₂I₃ perovskite films, which exhibit high responsivity and ultralow power density detection limit. Combining with the photolithography and surface functionalization, the large-scale CsCu₂I₃ perovskite film arrays are obtained through a vacuum-heating-assisted drop-casting patterning (VHADP) process with controllable morphology and homogenous dimension. These CsCu₂I₃ film arrays exhibit excellent air stability and resistance to photodegradation, whose X-ray diffraction (XRD) pattern won't change even under ambient condition for one month and their photoluminescence (PL) spectrum maintain stable after being illuminated for 8 h. The CsCu₂I₃-based flexible PDs array demonstrates outstanding optoelectronic performance with high responsivity, long-term stable dynamic photoresponse, and capability to resolve the weak UVC light intensity of 6.1 nW cm⁻². In addition, this flexible device shows a slight photocurrent decaying after either tensile or compressed bending and simultaneously detects the solar blind light distributions. Finally, a flame detection and warning system based on the CsCu₂I₃ film is fabricated, and it could be used for multi-flame detection and locating in a wide spatial angle range.

2. Results and Discussion

Figure 1a demonstrates the schematic illustration of the fabrication process of CsCu₂I₃ film arrays by the VHADP process. Briefly, the hydrophilic areas were obtained according to our previously reported method,^[28,40] and then CsCu₂I₃ films with desired patterns and shapes were grown by drop-casting the precursor solution and controlled crystallization process. Different crystallization methods were utilized to synthesize CsCu₂I₃ film arrays, including the one-step spin-coating and heating-assisted crystallization in air and vacuum conditions. As shown in Figure S1a (Supporting Information), the dendrite crystals were formed in the hydrophilic areas in the spin-coating method, indicating the uncontrolled crystallization process, while the small amount of precursor solutions leads to the poor coverage of the film. The drop-casting method ensures excess precursor solution in each pixel area and the high temperature speeds up the crystallization process, however, the grain size is small and vacancies are observed (Figure S1b, Supporting Information). Through the further introduction of the vacuum condition to regulate the nucleation density and crystallization rate, the flat and dense polycrystalline films were fabricated (Figure S1c, Supporting Information). The thickness of the CsCu₂I₃ film is ~200 nm (Figure S2, Supporting Information).

Various patterns and large-scale pixelated films with distinct boundaries were successfully prepared through the VHADP method. Figure 1b presents the scanning electron microscopy (SEM) images of the CsCu₂I₃ arrays with different shapes and dimensions, which possess homogenous morphology and clear edges. A complex logo of Guangxi University is also demonstrated by generating square pixel voids in a whole CsCu₂I₃ film with a pixel resolution of 100 μ m (Figure 1c; Figure S3, Supporting Information). Under the UV light excitation with a wavelength of 305 nm, a bright yellow fluorescence image of the logo was captured (Figure 1d). Different from the direct band emission in the Pb-based perovskites, this big mismatch between the yellow emission wavelength of CsCu₂I₃ film and its wide bandgap indicate the unique crystal structure and fluorescence mechanism.^[31,41] The composition and crystal structure of the as-fabricated CsCu₂I₃ array were further characterized through energy dispersive spectroscopy (EDS) and XRD. As shown in Figure 1e, the CsCu₂I₃ film demonstrated a compact surface with a large grain size, and all three elements were uniformly distributed throughout the film. The XRD results confirm the orthorhombic crystal structure (space group of cmcm) of the CsCu₂I₃ array. As shown in Figure 1f, the strong diffraction peaks of the CsCu₂I₃ array are observed at 10.81°, 21.64°, 21.98°, 27.12°, 42.92°, and 44.02°, which are consistent with the PDF#45-0076, and there are no peaks of impurity phases, proving the excellent crystallinity of the CsCu₂I₃ array through the VHADP method. The chemical composition is further verified via X-ray photoelectron spectroscopy (XPS). The Cs, Cu, and I elements are observed from the full-scan XPS spectra (Figure S4a, Supporting Information). Figure S4b,c (Supporting Information) exhibit the enlarged XPS spectra of I 3d (619.4 eV and 630.9 eV) and Cs 3d (724.4 eV and 738.4 eV). Moreover, the valency of Cu in the CsCu₂I₃ array was demonstrated in Figure 1g. Two distinct peaks at 932.5 eV and 952.3 eV are indexed to the Cu(I) 2p_{1/2} and Cu(I) 2p_{3/2}, suggesting that

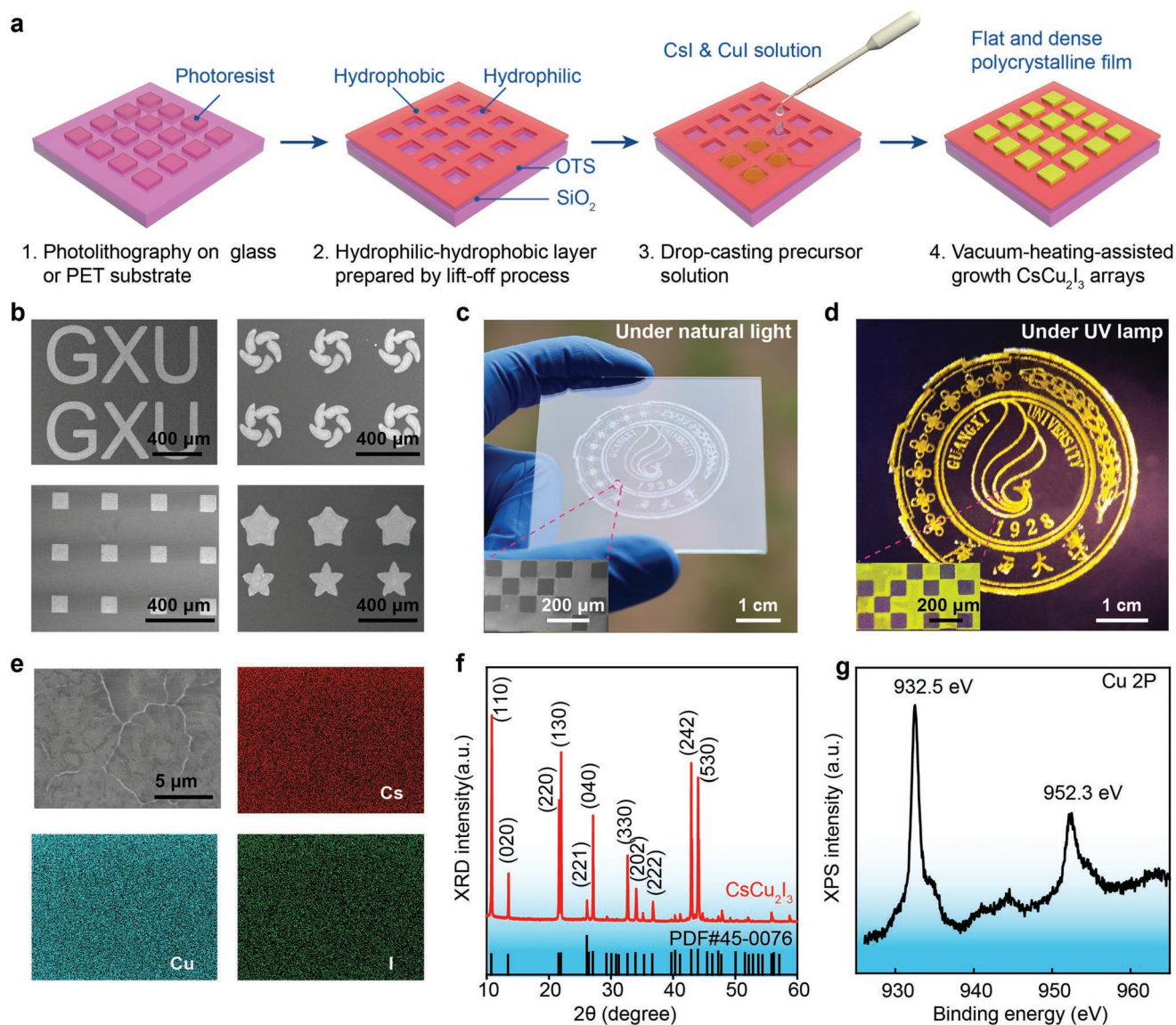


Figure 1. Preparation process and characterization of patterned CsCu_2I_3 films. a) Schematic illustration of the fabrication procedure for the controlled growth the CsCu_2I_3 film. b) SEM images of different patterns of CsCu_2I_3 films synthesized by the VHADP process. Photograph of large-scale pixelated patterns obtained by one-step solution process (c), which could emit yellow fluorescence with the irradiation of 254 nm (d). Element distribution analysis (e) and XRD patterns (f) of CsCu_2I_3 films. g) XPS analysis of the Cu element, which shows the Cu(I) in the CsCu_2I_3 films.

VHADP process can effectively protect the Cu(I) from being oxidized to Cu(II).^[29]

Optical properties of CsCu_2I_3 arrays were investigated by steady-state UV–Vis absorption, PL, PL excitation (PLE), and time-resolved PL (TRPL) spectra. The CsCu_2I_3 arrays demonstrate a sharp absorption band in the DUV region and a distinct absorption peak at 314 nm, and it could be attributed to the excitonic absorption, which coincides with the PLE spectrum (Figure 2a). The corresponding Tauc plot of the absorption spectrum reveals that CsCu_2I_3 film possesses a direct bandgap of 3.74 eV (Figure S5, Supporting Information). The band structure and density of states (DOS) of the CsCu_2I_3 film are further verified by density functional theory (DFT) calculation with the hybrid PBE functional. As shown in Figure 2b,

CsCu_2I_3 exhibits a direct bandgap of 3.70 eV at the Γ point, which is consistent with the absorption spectrum. For the state density, the conduction band minimum (CBM) of CsCu_2I_3 is primarily composed of Cu 4s, I 4d and Cs 5d orbitals, while the valence band maximum (VBM) mainly involves Cu 3d and I 5p orbitals. Inconsistent with the bandgap estimated from the absorption spectrum, the PL spectrum displays an emission peak centered at 580 nm with a broad full width at half maximum (FWHM) of 124 nm, showing a large Stokes shift of 266 nm (Figure 2a). Through fitting the TRPL decaying process of CsCu_2I_3 by an exponential function, an average exciton lifetime of 50 ns can be extracted (Figure 2c). Furthermore, the PL peak is independent of the excitation wavelength. As shown in Figure 2d, the peak is centered at 580 nm with an

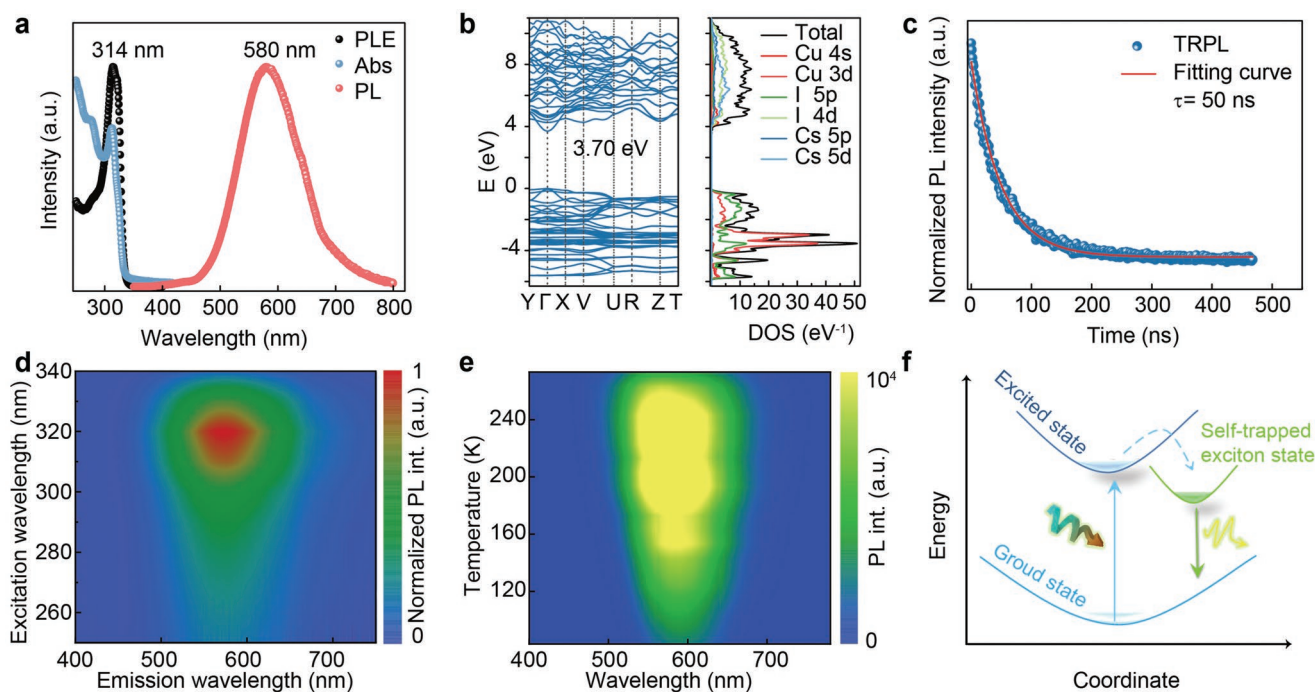


Figure 2. Optical properties of CsCu₂I₃ films array. a) Absorption, PLE, and PL spectra of CsCu₂I₃ film on glass substrate at room temperature. b) The electronic band structures and DOS of CsCu₂I₃ based on the DFT calculation, and the direct band gap (3.70 eV) is consistent with the absorption spectrum. c) TRPL decay spectrum of CsCu₂I₃ films, and the fitted curve shows the exciton lifetime is 50 ns. Excitation-dependent d) and temperature-dependent e) PL spectra of CsCu₂I₃ films. f) Configuration coordinate diagram of the formation of self-trapping excitons in the CsCu₂I₃ films.

excitation wavelength varying from 250 to 340 nm, while the emission intensity reaches the peak under the excitation wavelength of ~ 320 nm, which indicates the radiative recombination at different excitation wavelengths is originate from the same mechanism. Temperature-dependent PL further proves that the yellow fluorescence is derived from CsCu₂I₃, rather than other impurity phases. As the temperature increases from 83 to 273 K, there is only one emission center at ~ 580 nm (Figure 2e). The abnormal PL behaviors of CsCu₂I₃ films can be explained by the self-trapped exciton emission mechanism. According to the XRD analysis results, the orthorhombic crystal structure of CsCu₂I₃ is illustrated in Figure S6 (Supporting Information). Along the *c*-axis of the CsCu₂I₃ crystal, Cu⁺ is coordinated by four I⁻ to form a tetrahedron of [CuI₄]³⁻, and the shared edge tetrahedron forms a 1D chain structure. 1D cuprous iodide double chain is isolated by Cs atoms to produce a natural 1D electronic structure. Upon photoexcitation, the excitons are formed inside the CsCu₂I₃ crystal by the strong Coulomb interaction, which can generate large electroacoustic interaction due to the large ionicity of the 1D chain structure to introduce a large lattice distortion and band bending.^[41–44] Once the lattice distortion energy is high, the excitons tend to be immovable and get trapped to form self-trapped excitons, as shown in Figure 2f. Thus, based on the energy band theory, the large Stokes and yellow fluorescence of CsCu₂I₃ films can be explained by the self-trapping exciton process.

A flexible solar-blind PD array was then fabricated based on the CsCu₂I₃ film as the active layer through the VHADP method. Figure 3a shows the device structure of a representative pixel, consisting of the Au interdigital electrodes, a thin

layer of SiO₂ film for octadecyl trichlorosilane (OTS) treatment, and a layer of CsCu₂I₃ film. Considering the absorption of the DUV light by the polymer layer, we did not adopt the encapsulation layer and the as-fabricated device was exposed to air during the characterization process. The detailed fabrication procedures are schematically illustrated in Figure S7 (Supporting Information). Figure S8 (Supporting Information) shows the SEM images of the solar-blind PD arrays, where the CsCu₂I₃ film array was well aligned on the Au interdigital electrodes. To avoid crosstalk in the array device, a common electrode connected with one end of each pixel and the other end was separated. As shown in Figure 3b, a 10×10 array device was demonstrated on the PET substrate. According to the results of the DFT, the energy-level alignment diagram of the device is illustrated in Figure S9 (Supporting Information), showing that the Schottky junction is formed at the interface between CsCu₂I₃ and Au electrodes. The normalized response spectrum of the PDs array is presented in Figure 3c. The CsCu₂I₃-based PDs show a significant response for the solar-blind UV light (200–280 nm), and only respond to the wavelength region shorter than 336 nm (~ 3.70 eV), which is consistent with the calculated bandgap. Hence, the CsCu₂I₃-based PDs are suitable for the detection of solar-blind UV band, and further investigation is carried out with the deep UV light of the wavelength of 254 nm. Figure 3d presents the *I*–*V* curves of an individual pixel of the CsCu₂I₃ PDs array. The output current is 2.2 nA under 2 V bias in the dark condition, which increases to 3.2 and 21.3 nA with the illumination power density ranging from 0.005 to 0.388 mW cm⁻². The current–time curve was characterized under a wide range of illumination intensity. The device

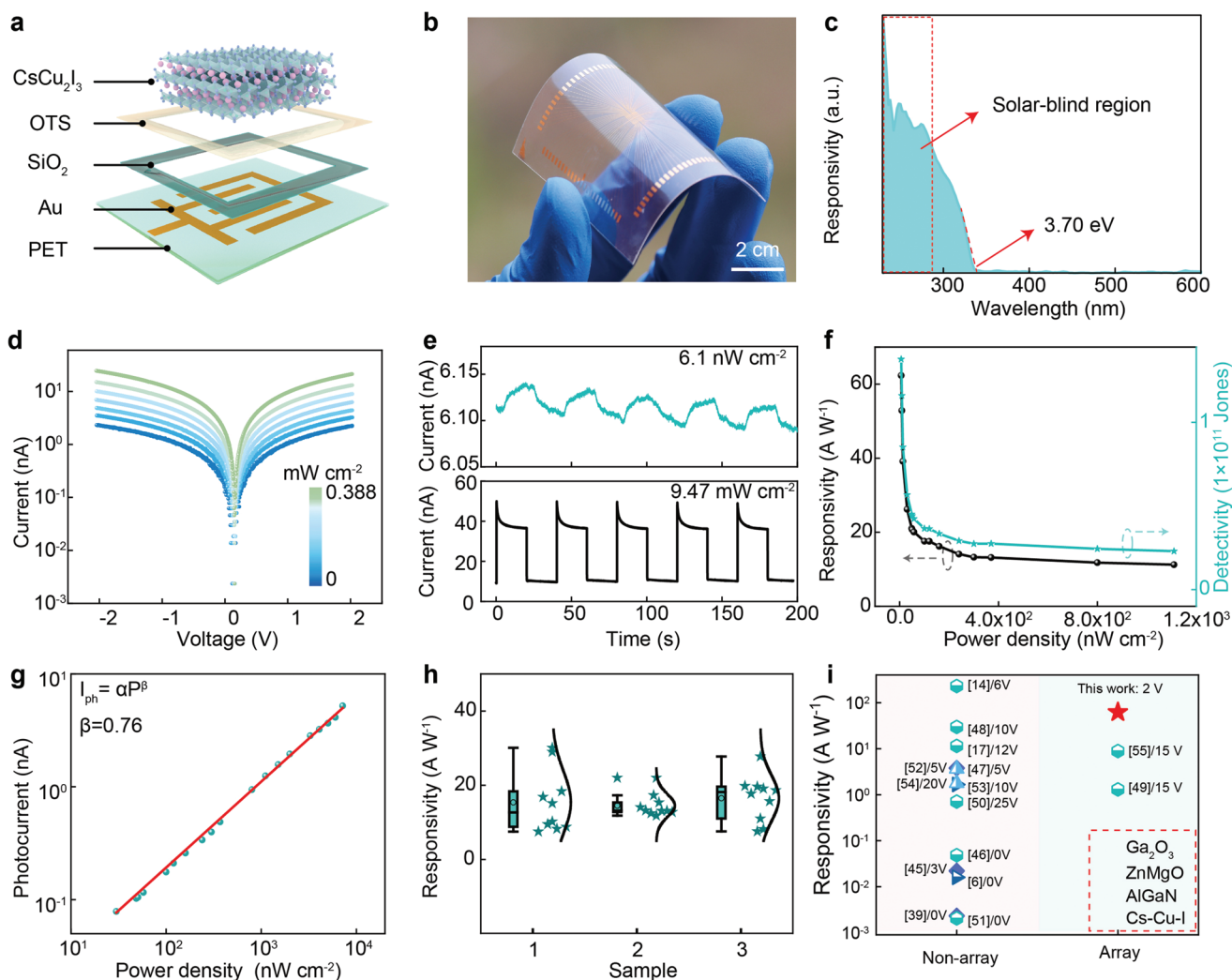


Figure 3. Optoelectronic performance of the solar-blind PDs array. a) Schematic illustration of the structure of the solar-blind PDs. b) Optical image of the 10×10 flexible solar-blind PDs array. c) Response spectrum of the solar-blind PDs array. d) I - V curves of the solar-blind PDs array measured in the dark or under DUV (254 nm) illumination with power density ranging from 0 to 0.388 mW cm^{-2} . e) Photoswitching properties of the solar-blind PDs array under the DUV illumination with power density of 6.1 nW cm^{-2} and 9.47 mW cm^{-2} . f) Responsivity and detectivity of the solar-blind PDs array with different power densities. g) The photocurrent versus illumination power density of the solar-blind PDs array. h) Statistical distribution of the responsiveness of 30 pixels at the illumination power density of 60 nW cm^{-2} . i) Comparison of responsivity for our solar-blind PDs array with previously reported devices.

demonstrates stable on/off switching behavior under both weak and strong illumination intensities of 6.1 nW cm^{-2} and 9.47 mW cm^{-2} , respectively (Figure 3e). Through calculating the time interval between the 10% and 90% of the values of the stable photocurrent, the response time of 13 ms and decay time of 19 ms are extracted (Figure S10, Supporting Information). Two critical parameters for the PDs, termed photoresponsivity (R) and detectivity (D^*), were calculated by the Equations 1 and 2:

$$R = \frac{I_{\text{light}} - I_{\text{dark}}}{PA} \quad (1)$$

$$D^* = \frac{RA^{1/2}}{(2eI_{\text{dark}})^{1/2}} \quad (2)$$

where I_{light} and I_{dark} are the photocurrent and dark current; P , e , and A are incident light power density, elementary charge, and effective area of an individual pixel, respectively. Figure 3f depicts the R and D^* of an individual pixel, representing a monotonic decay trend with the increase of light intensity. It is consistent with the conventional Pb-based perovskite PDs, which can be attributed to the high carrier recombination probability under the large illumination intensity. At the intensity of 6.1 nW cm^{-2} , R and D^* also reach their maximum values of 62 A W^{-1} and $1.4 \times 10^{11} \text{ Jones}$, respectively. Furthermore, intensity-dependent photocurrent data could be fitted by the following Equation 3:

$$I_{\text{ph}} = \alpha P^\beta \quad (3)$$

where I_{ph} is photocurrent ($I_{ph} = I_{light} - I_{dark}$), α is a proportional constant, and β is an exponent related to the recombination of photoexcited carriers. The fitting value of β is 0.76, exhibiting a small recombination loss and sublinear power-law behavior (Figure 3g). The statistics of the responsivity of 30 random pixels from three PD arrays are illustrated in Figure 3h. All the pixels demonstrate reliable photoresponse under the weak light intensity of 60 nW cm^{-2} with an average responsivity of 15.47 A W^{-1} , indicating an outstanding sensing capability for low-intensity solar-blind UV light. The comparison between our solar-blind PDs array and previously reported devices based on other materials is shown in Figure 3i.^[6,12,14,17,39,45–55] Our device array, which operates with a low bias voltage, demonstrates a high responsivity and excellent capability for weak light sensing. Considering the large-scale array configuration, it is much more competitive than previously single devices for practical applications.

The stability of the CsCu_2I_3 films array and flexible PDs were then characterized. It should be mentioned that both the perovskite films and PDs are functionalized without encapsulation. We first characterized the structural stability of the CsCu_2I_3 films array. As shown in Figure 4a, under continuous UV irradiation for 8 h, the center wavelength of the PL peak maintained unchanged and only a slight decay was observed for PL intensity. The crystal structure of the CsCu_2I_3 films was also measured after being exposed to ambient conditions for one month (Figure 4b). There is no change in the XRD peaks and no new diffraction signals are observed. The PL and XRD results prove the excellent resistance to photodegradation and

outstanding structure stability in the air. Then, the mechanical robustness of the flexible PDs array was measured under different bending conditions. The experimental setup of the bending test is illustrated in Figure S11 (Supporting Information). Under the compression condition, both the photocurrent and dark current remain almost unchanged with increasing the bending angle to 30° (Figure 4c; Figure S11, Supporting Information). However, the photocurrent demonstrates a sharp decrease in the tension condition, which may be due to the surface cracks introduced by the large tensile strain of the CsCu_2I_3 films that are out of the neutral plane. It is worth noting that the device can maintain stable on/off switching behavior with fast response under different bending angles. Figure 4d shows the statistical results of the output current of 20 independent pixels under different bending cycles with the compression bending angle of 30° , and the dark current and photocurrent can be well preserved, suggesting excellent mechanical stability under compressive strain. The long-term stability of the photo-switching behavior is performed with a periodic UV illumination with 5 s for light on and off, respectively. As shown in Figure 4e, the device can be operated steadily under continuous illumination for 8 h, confirming the excellent resistance to photodegradation of the CsCu_2I_3 film.

High performance PDs array with imaging capability is one of the crucial components in large-scale optoelectronic systems. Our flexible PDs array could reconstruct solar-blind UV images through mapping the output current from each pixel and the data acquisition setup is illustrated in Figure 5a. The uniform deep UV light was applied to the PDs array

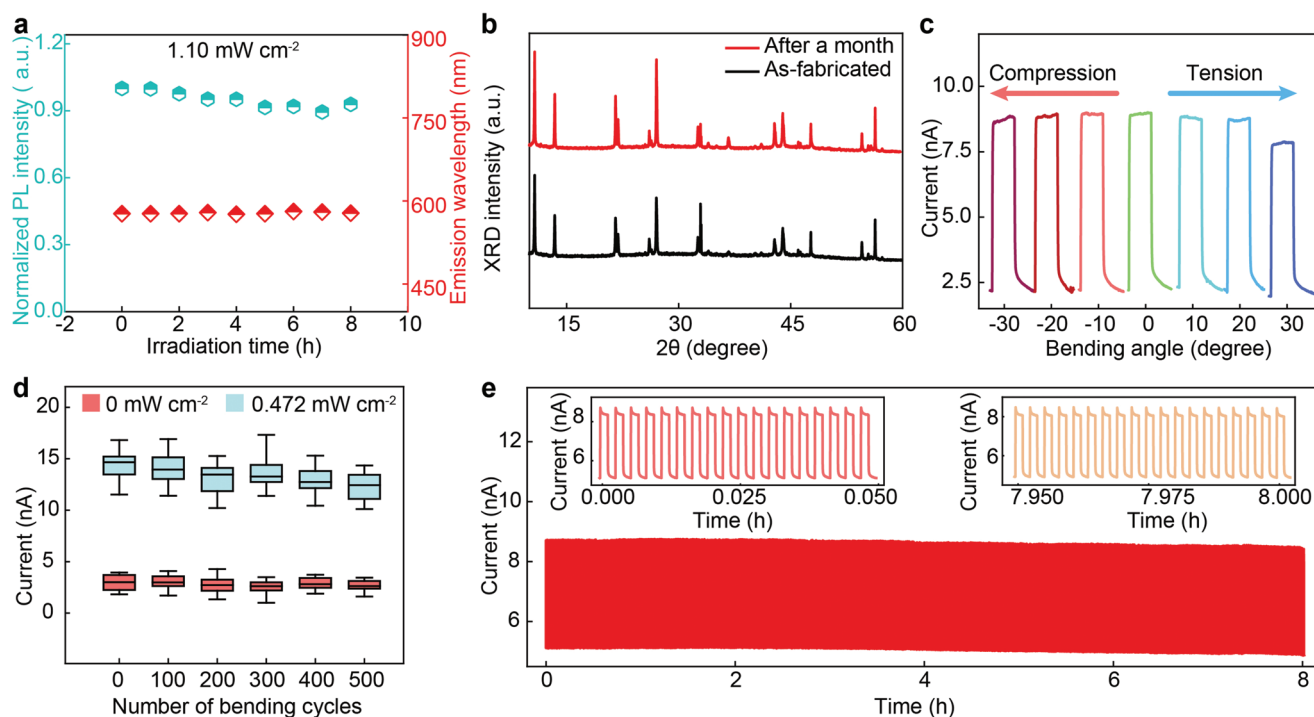


Figure 4. Stability of CsCu_2I_3 films and solar-blind PDs array. a) Photostability of the CsCu_2I_3 films under continuous irradiation (314 nm , 1.10 mW cm^{-2}) for 8 h. b) XRD of the CsCu_2I_3 films exposed to air for one month. c) The on/off switching behavior of the solar-blind PDs array with different compression and tension bending angles. d) Statistical distribution of the dark current and photocurrent of 20 pixels after different bending cycles. e) Working stability of the solar-blind PDs array under the bias voltage of 2 V after the on/off switch for 8 h.

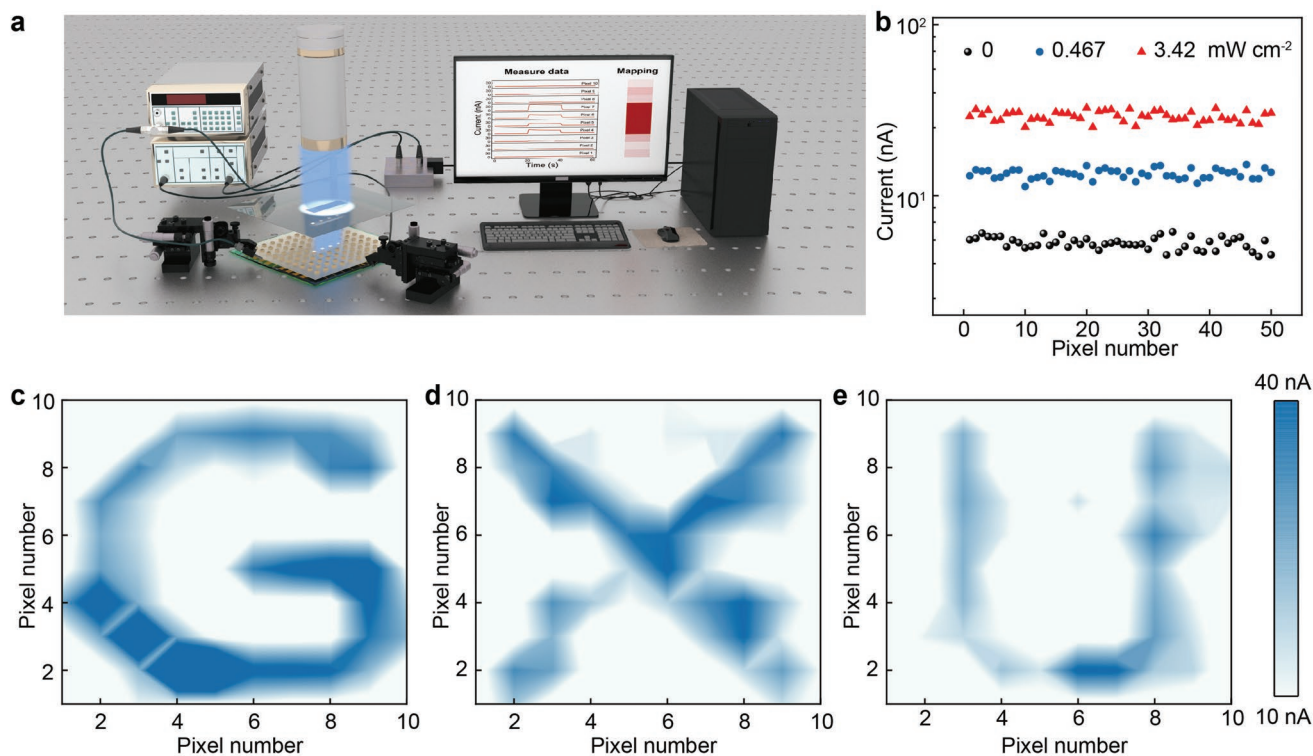


Figure 5. Imaging performance of solar-blind PDs array. a) Schematic diagram of the experimental setup for the imaging test. b) Output currents of 50 pixels at the powerdensities of 0, 0.467, and 3.42 mW cm^{-2} . c–e) DUV light intensity mapping by the solar-blind PDs array with different masks.

through a predesigned shadow mask, and a digital source-meter unit interfaced with a computer was used to measure and record the real-time current of the individual pixel. The selectivity and uniformity of the array device are crucial for reconstructing clear images. As shown in Figure S12 (Supporting Information), the deep UV light was applied on the selected 4 pixels and the output current of all the 10 pixels in one column (red dashed box) were collected synchronously. Obviously, each pixel works independently and only the illuminated pixels demonstrate a significant current change, confirming the free crosstalk of the PDs array. Figure 5b summarizes the output current of 50 pixels in the PDs array with the illumination intensity of 0, 0.467, and 3.42 mW cm^{-2} , respectively. The histogram shows the currents are distributed in the narrow ranges of 5.1 ± 0.5 nA, 13.4 ± 0.5 nA, and 29.1 ± 0.5 nA, respectively (Figure S13, Supporting Information). These results suggest the flexible PDs array possesses satisfactory uniformity under different illumination intensities. In addition, through mapping the output current of all the 100 pixels of the PDs array, the DUV light distribution can be obtained. As shown in Figure 5c–e, the clear letters “G”, “X”, and “U” could be easily identified, indicating its high imaging capability for solar-blind UV light detection.

A flame detection and warning system was further explored based on the capability of ultra-weak light detection. As shown in Figure 6a, the system consists of a curved PDs array, a signal emission unit, and a router. The curved PDs array was designed with 40 pixels in a simple origami method, which are uniformly distributed on 8 arms, and was bent into a hemispherical configuration with a diameter of 6 cm. It can achieve the detection

of multiple flame signals with a wide angle range of 0° – 180° and locate the flames through mapping the output current intensity. The flame information can be uploaded to the WLAN in real time, and multiple clients (phones, tablets, watch, or other smart terminals) can monitor the signal synchronously. Figure 6b shows the image of the flame detection and warning system. While the photocurrent of the PDs array exceeds the set threshold, the measured data could be uploaded to the cloud service, and then different users could receive the fire alarm and check the data in real time (details could be found in Movie S1, Supporting Information). The system demonstrates good selectivity of the flame signal. As shown in Figure 6c, under either the illumination of a fluorescent lamp or the dark condition, the output currents of the system used to detect the flame of an alcohol lamp show no obvious change, indicating the negligible background interference of the system. In addition, the locations of the flames could also be identified by the system. As shown in Figure 6d–i, 40 pixels are distributed on the weft and wrap lines of the hemisphere. Specifically, 8 arms of the curved PDs array are labeled as A–H in a counter-clockwise direction and five PDs on each arm are marked from 1 to 5. The flame irradiation ($220 \mu\text{W cm}^{-2}$) is close to position A5. The current distribution of the curved PDs array is shown in Figure 6d–ii, showing that the pixels adjacent to A5 demonstrate an obvious photocurrent increase, while the other pixels (for example, pixels on wrap C–D) maintain in a dark current state. Thus, the flame location could be extracted through the 3D current distribution mapping (Figure 6e). The capability of the system for multi-flame detection is demonstrated in Figure 6f. Three

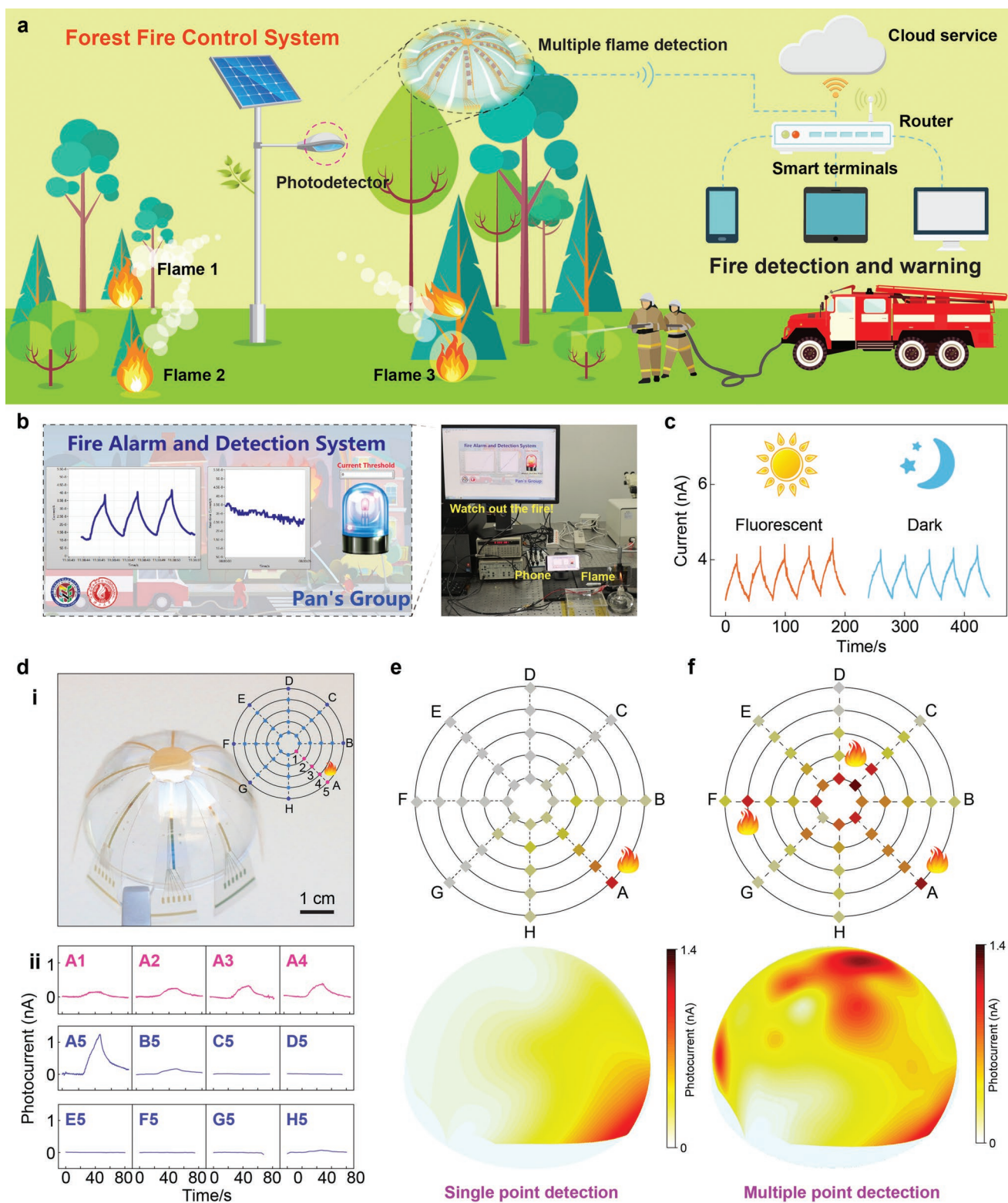


Figure 6. Flame detection and warning system based on a curved solar-blind PDs array applied in forest fire control system. **a)** Schematic diagram of multiple flame detection of curved solar-blind PDs array applied in forest fire control system. **b)** An interface of the developed flame detection and warning system (left), which could effectively detect the flame and transmit the data to the mobile phone for real-time monitoring (right). **c)** Photoswitching properties to the flame under a fluorescent lamp illumination (1.195 mW cm^{-2}) and dark environment, respectively. **d)** i) Digital image of curved solar-blind PDs array attached on the hemisphere support. Inset is the corresponding 2D plane diagram. ii) Current variation of the pixels at different positions with the flame ($220 \mu\text{W cm}^{-2}$) close to the A5 pixel. Current distribution of the curved solar-blind PDs array under single flame **e)** and multi-flame **f)** irradiation.

flames located in different spatial directions were used around the curved PDs array simultaneously. Through mapping the photocurrent, the system could identify the flames next to positions A5, C2, and F4. This system could be used for flame warning and locating, which will play an important role in the understanding of flame conditions and firefighting planning.

3. Conclusion

In summary, the CsCu₂I₃ films array was successfully synthesized by the VHADP process with controlled shapes, dimensions, and compact surfaces. It could emit bright yellow fluorescence due to the mechanism of self-trapped excitons. Furthermore, the flexible solar-blind PDs array based on the CsCu₂I₃ film pattern was demonstrated on the PET substrate, which achieves a wide power density detection range and shows obvious advantages in the ultralow-power density detection. It can resolve the ultraweak light intensity of 6.1 nW cm⁻² with a high responsivity of 62 A W⁻¹. The PDs array also demonstrates long-term working stability with little attenuation in performance after continuous working for 8 h and it can realize the real-time solar-blind UV light distribution. By employing the origami design, the flexible PDs array could be bent into a hemispherical configuration for multi-flame warning and locating. Hence, our research has demonstrated the potential application of copper halide perovskite PDs array in the field of solar-blind detection, which will be the essential components in space communications, missile warning, and flame alerting applications.

4. Experimental Section

Materials: Copper iodide (CuI 99.95%), Cesium iodide (CsI 99.999%), N,N-Dimethylformamide (DMF 99.5%), and Dimethyl sulfoxide (DMSO >99%) were purchased from Aladdin. (octadecyl) trichlorosilane (OTS 95%) was purchased from Macklin. Acetone was purchased from Xilong Scientific and n-hexane was purchased from Yongda Chemical. All the chemicals were used as received without further purification.

Fabrication of the Hydrophilic Patterns on the PET Substrate: First, the PET substrate was treated with oxygen plasma to generate a hydrophilic surface (100 W, 0.1 mTorr, and 300 s). A positive photoresist was spin-coated on its surface (S1813, 4000 r min⁻¹, and 30 s), and the different photoresist patterns were obtained via photolithography, which could be used to define the shape and dimension of the CsCu₂I₃ films. Then, the SiO₂ film was deposited on the substrate by magnetron sputtering followed by immersing it into a mixture of OTS and hexane (volume ratio 1:100) for 20 min to generate a hydrophobic surface. Finally, photoresist patterns were removed in acetone for 5 min.

Synthesis of CsCu₂I₃ Films Array: DMF and DMSO were mixed with a volume ratio of 4:1 as the solvent. CsI and CuI with a mole ratio of 1:2 were dissolved in the DMF and DMSO mixture. Subsequently, a PTFE filter was used to filter the yellow-brown precursor solution, and then the solution was drop-casted on the pretreated substrate, leaving the solution only in the hydrophilic areas. Finally, the substrate was put into a vacuum drying oven at 40 °C for the controlled CsCu₂I₃ crystallization.

Fabrication of CsCu₂I₃ PDs Array: A 0.188 mm-thick PET film was employed as the flexible substrate. The Au electrodes were fabricated through conventional photolithography, magnetron sputtering deposition, and photoresist lift-off process. Then, the as-fabricated substrate was treated with the hydrophilic process to generate hydrophilic patterns, followed by the CsCu₂I₃ films synthesis on the desired positions.

Density Functional Theory Calculations: Electronic properties of the CsCu₂I₃ were analyzed by first-principles (FP) calculations within the Atomistic Tool Kit (ATK Version R-2020.09) package using the projector augmented wave (PAW) method. The exchange and correlation potentials were treated with Perdew-Burke-Ernzerhof (PBE) generalized gradient approximation (GGA). In addition, the hybrid functional HSE06 was also employed to obtain more reliable electronic band structures and density of states (DOS). The linear combination of atomic orbitals (LCAO) basis set with high accuracy and Gaussian smearing occupation method were used for the structures. Energy convergence of the calculations was ensured by setting a density mesh cutoff of 105 Hartree with a 4 × 4 × 5 k-mesh sampling in the Brillouin zone (BZ). The cells had been fully relaxed and optimized with the Limited-memory Broyden-Fletcher-Goldfarb-Shanno (LBFGS) optimizer until a maximum force of 0.02 eV Å⁻¹ per atom.

Bending Test System: The PDs were attached to the flexible PET substrates and then were mounted on a customized acrylic holder. One end of the device was fixed on a 3D stage, and the other end was fixed to a movable linear motor (LinMot E1100). Through controlling the movement of the motor, different bending angles and bending cycles of the device could be achieved. Output currents of the PDs were obtained using the semiconductor parameter analyzer (Keithley 4200) and a probe station (Semiprobe M-6).

Flame Detection and Warning System: The 8 × 5 array devices were fabricated on the circular PET according to the concentric circles at 45° angular intervals, and the specific fabrication method was as described above. Use the simple origami method to remove the unnecessary parts and attach the device to a hemisphere support with scotch tape, which could be used for multi-flame detection. Moreover, the photocurrent measured by the data acquisition system was analyzed by the self-made LabVIEW program, then different current thresholds were set to achieve flame detection. The corresponding analysis results could be uploaded to the WLAN through the web server, and various mobile terminals could log in webpage to realize multiple real-time monitoring.

Characterization and Measurements: The morphologies and EDS images of the synthesized CsCu₂I₃ arrays were obtained by field emission scanning electron microscopy (FEI Nova NanoSEM 450). The XPert3 Powder X-ray diffractometer with a Cu Kα radiation was used to analyze the crystallinity of the CsCu₂I₃ films, and the valency of Cu element in the films was analyzed by XPS (Thermo Scientific, K-alpha). The absorption spectra were measured by the UV-VIS-NIR spectrometer of Shimadzu UV3600. Photoluminescence and excitation spectra were acquired by Edinburgh FLS980 with a Fluoracore Software system. The response spectrum was analyzed through a customized response spectrum test system, including Xe Lamp, monochromator, chopper, and phase-locked amplifier. Temperature-dependent PL was measured by a system of a temperature controller and focus on excellence of mK 2000 and KSUL 1 708 229 system. I-V and I-T data were measured by a function generator and a current preamplifier (Stanford DS 345 and SR 570).

Supporting Information

Supporting Information is available from the Wiley Online Library or from the author.

Acknowledgements

The authors thank the support of National Natural Science Foundation of China (No. 52125205, U20A20166, 61805015 61804011 and 52102184), Natural Science Foundation of Beijing Municipality (Z180011), Shenzhen Science and Technology Program (Grant No. KQTD20170810105439418), the Fundamental Research Funds for the Central Universities and GuangDong Basic and Applied Basic Research Foundation (2020A1515110740).

Conflict of Interest

The authors declare no conflict of interest.

Data Availability Statement

Research data are not shared.

Keywords

CsCu₂I₃, flame detection, lead-free perovskite, solar-blind photodetectors

Received: January 12, 2023

Revised: February 27, 2023

Published online:

- [1] C. Zou, Q. Liu, K. Chen, F. Chen, Z. Zhao, Y. Cao, C. Deng, X. Wang, X. Li, S. Zhan, F. Gao, S. Li, *Mater. Horiz.* **2022**, *9*, 1479.
- [2] X. Chen, F. Ren, S. Gu, J. Ye, *Photonics Res.* **2019**, *7*, 381.
- [3] H. Chen, K. Liu, L. Hu, A. A. Al-Ghamdi, *X. Fang, Mater. Today* **2015**, *18*, 493.
- [4] C. Xie, X. T. Lu, X. W. Tong, Z. X. Zhang, F. X. Liang, L. Liang, L. B. Luo, Y. C. Wu, *Adv. Funct. Mater.* **2019**, *29*, 1806006.
- [5] D. H. Wang, X. Liu, S. Fang, C. Huang, Y. Kang, H. B. Yu, Z. L. Liu, H. C. Zhang, R. Long, Y. J. Xiong, Y. J. Lin, Y. Yue, B. H. Ge, T. K. Ng, B. S. Ooi, Z. T. Mi, J. H. He, H. D. Sun, *Nano Lett.* **2021**, *21*, 120.
- [6] M. M. Fan, K. W. Liu, X. Chen, Z. Z. Zhang, B. H. Li, D. Z. Shen, *RSC Adv.* **2017**, *7*, 13092.
- [7] J. B. Lu, Z. S. Lv, X. J. Qiu, S. Q. Lai, H. Jiang, *Photonics Res.* **2022**, *10*, 2229.
- [8] H. C. Zhang, F. Z. Liang, K. Song, C. Xing, D. H. Wang, H. B. Yu, C. Huang, Y. Sun, L. Yang, X. L. Zhao, H. D. Sun, S. B. Long, *Appl. Phys. Lett.* **2021**, *118*, 242105.
- [9] Y. H. Pu, Y. C. Liang, *Appl. Phys. Lett.* **2022**, *121*, 062105.
- [10] C. J. Collins, U. Chowdhury, M. M. Wong, B. Yang, A. L. Beck, R. D. Dupuis, J. C. Campbell, *Appl. Phys. Lett.* **2002**, *80*, 3754.
- [11] Y. N. Hou, Z. X. Mei, Z. L. Liu, T. C. Zhang, X. L. Du, *Appl. Phys. Lett.* **2011**, *98*, 103506.
- [12] Y. Chen, Y. Lu, M. Liao, Y. Tian, Q. Liu, C. Gao, X. Yang, C. Shan, *Adv. Funct. Mater.* **2019**, *29*, 1906040.
- [13] L. X. Qian, Z. W. Gu, X. D. Huang, H. Y. Liu, Y. J. Lv, Z. H. Feng, W. L. Zhang, *ACS Appl. Mater. Interfaces* **2021**, *13*, 40837.
- [14] Y. Qin, L. H. Li, X. L. Zhao, G. S. Tompa, H. Dong, G. Z. Jian, Q. M. He, P. J. Tan, X. H. Hou, Z. F. Zhang, S. J. Yu, H. D. Sun, G. W. Xu, X. S. Miao, K. H. Xue, S. B. Long, M. Liu, *ACS Photonics* **2020**, *7*, 812.
- [15] C. Chen, X. L. Zhao, X. H. Hou, S. J. Yu, R. Chen, X. Z. Zhou, P. J. Tan, Q. Liu, W. X. Mu, Z. T. Jia, G. W. Xu, X. T. Tao, S. B. Long, *IEEE Electron Device Lett.* **2021**, *42*, 1492.
- [16] J. Y. Lai, M. N. Hasan, E. Swinnich, Z. Tang, S. H. Shin, M. Kim, P. H. Zhang, J. H. Seo, *J. Mater. Chem. C* **2020**, *8*, 14732.
- [17] X. H. Hou, H. D. Sun, S. B. Long, G. S. Tompa, T. Salagaj, Y. Qin, Z. F. Zhang, P. J. Tan, S. J. Yu, M. Liu, *IEEE Electron Device Lett.* **2019**, *40*, 1483.
- [18] K. Xia, W. Wu, M. Zhu, X. Shen, Z. Yin, H. Wang, S. Li, M. Zhang, H. Wang, H. Lu, A. Pan, C. Pan, Y. Zhang, *Sci. Bull.* **2020**, *65*, 343.
- [19] J. L. Sun, Q. L. Hua, M. Q. Zhao, L. Dong, Y. Chang, W. Q. Wu, J. Li, Q. S. Chen, J. G. Xi, W. G. Hu, C. F. Pan, C. X. Shan, *Adv. Mater. Technol.* **2021**, *6*, 2100229.
- [20] F. Li, Z. G. Xia, C. F. Pan, Y. Gong, L. Gu, Q. L. Liu, J. Z. Zhang, *ACS Appl. Mater. Interfaces* **2018**, *10*, 11739.
- [21] S. D. Stranks, G. E. Eperon, G. Grancini, C. Menelaou, M. J. P. Alcocer, T. Leijtens, L. M. Herz, A. Petrozza, H. J. Snaith, *Science* **2013**, *342*, 341.
- [22] C. Wehrenfennig, G. E. Eperon, M. B. Johnston, H. J. Snaith, L. M. Herz, *Adv. Mater.* **2014**, *26*, 1584.
- [23] M. A. Green, A. Ho-Baillie, H. J. Snaith, *Nat. Photonics* **2014**, *8*, 506.
- [24] J. H. Noh, S. H. Im, J. H. Heo, T. N. Mandal, S. I. Seok, *Nano Lett.* **2013**, *13*, 1764.
- [25] Y. Z. Zhu, J. P. Chen, Q. N. Cui, H. Guo, Z. X. Li, Z. L. Shi, C. X. Xu, *Nano Res.* **2021**, *14*, 4288.
- [26] X. Han, W. Q. Wu, H. Chen, D. F. Peng, L. Qiu, P. G. Yan, C. F. Pan, *Adv. Funct. Mater.* **2021**, *31*, 2005230.
- [27] W. Q. Wu, M. M. Zhou, D. Li, S. M. Li, Z. Yang, Z. H. Huo, Y. Q. Wu, Y. W. Tan, X. Han, C. F. Pan, A. N. Pan, *Nanoscale* **2021**, *13*, 9177.
- [28] W. Q. Wu, X. D. Wang, X. Han, Z. Yang, G. Y. Gao, Y. F. Zhang, J. F. Hu, Y. W. Tan, A. L. Pan, C. F. Pan, *Adv. Mater.* **2019**, *31*, 1805913.
- [29] P. F. Cheng, L. Sun, L. Feng, S. Q. Yang, Y. Yang, D. Y. Zheng, Y. Zhao, Y. B. Sang, R. L. Zhang, D. H. Wei, W. Q. Deng, K. L. Han, *Angew. Chem. Int. Ed.* **2019**, *58*, 16087.
- [30] T. Li, X. M. Mo, C. Y. Peng, Q. C. Lu, C. J. Qi, X. M. Tao, Y. F. Ouyang, Y. L. Zhou, *Chem. Commun.* **2019**, *55*, 4554.
- [31] X. Mo, T. Li, F. Huang, Z. Li, Y. Zhou, T. Lin, Y. Ouyang, X. Tao, C. Pan, *Nano Energy* **2021**, *81*, 105570.
- [32] W. Liu, K. W. Ng, H. Lin, Z. Dai, J. Xu, S. Su, Z. Tang, S. Wang, *J. Phys. Chem. C* **2021**, *125*, 13076.
- [33] K. J. Kwak, J. H. Baek, D. E. Lee, I. H. Im, J. Kim, S. J. Kim, Y. J. Lee, J. Y. Kim, H. W. Jang, *Nano Lett.* **2022**, *22*, 6010.
- [34] S. L. Cheng, A. Beitlerova, R. Kucerkova, M. Nikl, G. H. Ren, Y. T. Wu, *Phys. Status Solidi-Rapid Res. Lett.* **2020**, *14*, 2000374.
- [35] M. Y. Zhang, J. S. Zhu, B. Yang, G. D. Niu, H. D. Wu, X. Zhao, L. X. Yin, T. Jin, X. Y. Liang, J. Tang, *Nano Lett.* **2021**, *21*, 1392.
- [36] X. Y. Zhou, L. C. Zhang, Y. Huang, Z. Y. Zhou, W. Q. Xing, J. Zhang, F. W. Zhou, D. Y. Zhang, F. Z. Zhao, *Adv. Opt. Mater.* **2021**, *9*, 2100889.
- [37] Z. S. Luo, Q. Li, L. M. Zhang, X. T. Wu, L. Tan, C. Zou, Y. J. Liu, Z. W. Quan, *Small* **2020**, *16*, 1905226.
- [38] Z. X. Zhang, C. Li, Y. Lu, X. W. Tong, F. X. Liang, X. Y. Zhao, D. Wu, C. Xie, L. B. Luo, *J. Phys. Chem. Lett.* **2019**, *10*, 5343.
- [39] J. Ma, X. Xia, S. Yan, Y. Li, W. Liang, J. Yan, X. Chen, D. Wu, X. Li, Z. Shi, *ACS Appl. Mater. Interfaces* **2021**, *13*, 15409.
- [40] W. Q. Wu, X. Han, J. Li, X. D. Wang, Y. F. Zhang, Z. H. Huo, Q. S. Chen, X. D. Sun, Z. S. Xu, Y. W. Tan, C. F. Pan, A. L. Pan, *Adv. Mater.* **2021**, *33*, 2006006.
- [41] Y. Hui, S. Chen, R. Lin, W. Zheng, F. Huang, *Mat. Chem. Front.* **2021**, *5*, 7088.
- [42] X. Zhao, G. D. Niu, J. S. Zhu, B. Yang, J. H. Yuan, S. R. Li, W. R. Gao, Q. S. Hu, L. X. Yin, K. H. Xue, E. Lifshitz, X. S. Miao, J. Tang, *J. Phys. Chem. Lett.* **2020**, *11*, 1873.
- [43] Y. Gu, X. Yao, M. Long, H. Geng, M. Hu, *Mater. Lett.* **2022**, *323*, 132607.
- [44] Z. Z. Ma, Z. F. Shi, C. C. Qin, M. H. Cui, D. W. Yang, X. J. Wang, L. T. Wang, X. Z. Ji, X. Chen, J. L. Sun, D. Wu, Y. Zhang, X. J. Li, L. J. Zhang, C. X. Shan, *ACS Nano* **2020**, *14*, 4475.
- [45] J. Yang, W. Kang, Z. Z. Liu, M. Y. Pi, L. B. Luo, C. Li, H. Lin, Z. T. Luo, J. Du, M. Zhou, X. S. Tang, *J. Phys. Chem. Lett.* **2020**, *11*, 6880.
- [46] Y. C. Chen, X. Yang, C. Y. Zhang, G. H. He, X. X. Chen, Q. Qiao, J. H. Zang, W. J. Dou, P. X. Sun, Y. Deng, L. Dong, C. X. Shan, *Nano Lett.* **2022**, *22*, 4888.
- [47] J. A. Lv, X. Y. Lu, X. Li, M. X. Xu, J. S. Zhong, X. Zheng, Y. Q. Shi, X. F. Zhang, Q. Zhang, *Small* **2022**, *18*, 2201715.
- [48] S. Oh, C. K. Kim, J. Kim, *ACS Photonics* **2018**, *5*, 1123.

- [49] M. F. Ding, K. Liang, S. J. Yu, X. L. Zhao, H. H. Ren, B. W. Zhu, X. H. Hou, Z. W. Wang, P. J. Tan, H. Huang, Z. F. Zhang, X. L. Ma, G. W. Xu, S. B. Long, *Adv. Opt. Mater.* **2022**, *10*, 2200512.
- [50] S. L. Wang, H. L. Sun, Z. Wang, X. H. Zeng, G. R. Ungar, D. Y. Guo, J. Q. Shen, P. G. Li, A. P. Liu, C. R. Li, W. H. Tang, *J. Alloy. Compd.* **2019**, *787*, 133.
- [51] R. R. Zhuo, D. Wu, Y. G. Wang, E. P. Wu, C. Jia, Z. F. Shi, T. T. Xu, Y. T. Tian, X. J. Li, *J. Mater. Chem. C* **2018**, *6*, 10982.
- [52] S. C. Wu, M. J. Wu, Y. F. Chen, *ACS Appl. Nano Mater.* **2020**, *3*, 7595.
- [53] M. M. Fan, K. W. Liu, Z. Z. Zhang, B. H. Li, X. Chen, D. X. Zhao, C. X. Shan, D. Z. Shen, *Appl. Phys. Lett.* **2014**, *105*, 011117.
- [54] K. Jiang, X. J. Sun, Z. H. Zhang, J. W. Ben, J. M. Che, Z. M. Shi, Y. P. Jia, Y. Chen, S. L. Zhang, W. Lv, D. B. Li, *Photonics Res.* **2020**, *8*, 1243.
- [55] Y. C. Chen, Y. J. Lu, M. Y. Liao, Y. Z. Tian, Q. Liu, C. J. Gao, X. Yang, C. X. Shan, *Adv. Funct. Mater.* **2019**, *29*, 1906040.